

Controlling the $\{111\}/\{110\}$ surface Ratio of Cuboidal Ceria Nanoparticles

*Uli Castanet,^a Cédric Feral-Martin,^b Alain Demourgues,^a Rachel L. Neale,^c Dean C. Sayle,^c
Francesco Caddeo,^c Joseph M. Flitcroft,^d Robert Caygill,^d Ben J. Pointon,^d Marco Molinari,^{d,*}
and Jerome Majime^l^{a,*}*

^a CNRS, Univ. Bordeaux, ICMCB, UPR 9048, 87 Avenue du Docteur Schweitzer, 33600 Pessac,
France.

^b Solvay Silica, 52, rue de la Haie Coq, 93306 Aubervilliers, France

^c School of Physical Science, University of Kent, Canterbury, Kent, CT2 7NZ, United Kingdom

^d Department of Chemistry, University of Huddersfield, Huddersfield, HD1 3DH, United
Kingdom

Keywords: ceria nanocube, faceting, liquid-like catalysis, molecular modelling, ceria catalysis,
ceria nanoparticle

Abstract

The ability to control size and morphology is crucial in optimizing nanoceria catalytic activity as this is governed by the atomistic arrangement of species and structural features at the surfaces.

Here, we show that cuboidal cerium oxide nanoparticles can be obtained via microwave-assisted hydrothermal synthesis in highly alkaline media. HRTEM revealed that the cube edges were truncated by $\text{CeO}_2\{110\}$ surfaces and the cube corners by $\text{CeO}_2\{111\}$ surfaces. When adjusting synthesis conditions by increasing NaOH concentration, the average particle size increased. Although this was accompanied by an increase of the cube faces, $\text{CeO}_2\{100\}$, the cube edges, $\text{CeO}_2\{110\}$, and cube corners, $\text{CeO}_2\{111\}$ remained of constant size. Molecular Dynamics (MD) was used to rationalise this behaviour and revealed that energetically, the corners and edges cannot be atomically sharp, rather they are truncated by $\{111\}$ and $\{110\}$ surfaces respectively to stabilise the nanocube; both experiment and simulation agreed a minimum size of ~ 1.6 nm associated with this truncation. Moreover, HRTEM and MD revealed $\{111\}/\{110\}$ faceting of the $\{110\}$ edges, which balances the surface energy associated with the exposed surfaces, which follows $\{111\} > \{110\} > \{100\}$, although only the $\{110\}$ surface facets because of the ease of extracting oxygen from its surface, which follows $\{111\} > \{100\} > \{110\}$. Finally, MD revealed that the $\{100\}$ surfaces are ‘liquid-like’ with a surface oxygen mobility 5 orders of magnitude higher than that on the $\{111\}$ surfaces; this arises from the flexibility of the surface species network that can access many different surface arrangements due to very small energy differences.

This finding has implications for understanding the surface chemistry of nanoceria and provides avenues to rationalize the design of catalytically active materials at the nanoscale.

1. Introduction

Since the first nanoparticle syntheses, research has focused on producing various nano-catalysts of different compositions and applications¹⁻³. Over the years, the importance of their shape, hence their exposed facets, grew in interest⁴⁻⁶. The differences between facets, may sometimes remain unclear and controversial, but more and more effects in terms of reactivity and/or selectivity are shown in recent works^{5,7-12}. Furthermore different morphologies are active towards oxidative catalysis at different temperatures, with nanocubes exposing the {100} surfaces being active at temperatures as low as 150°C¹³.

CeO₂ is now well known for its catalytic redox properties¹⁴, associated or not with other materials (Au on a reconstructed ceria surface¹⁵ and other noble metals, TiO₂) especially towards CO oxidation, even at low temperature. After years of research, numerous shapes of ceria nanoparticles became available, as described in several papers^{6,15-22} like rods, octahedrons, cubes, *etc.*

Among those particle shapes, the rods seem to be the most reactive nanoscale morphology, mainly because of the inherent amount of defects and the exposed facets, which are extremely reactive^{18,23}. The exposed {110} surfaces of nanorods have been shown to undergo reconstruction, with {111}-type faceting, providing an explanation for the higher surface reactivity observed²⁰. However, these morphologies are so reactive that they tend to evolve under catalytic conditions, lowering or even inhibiting reactivity, by encapsulation of deposited precious metals and co-catalysts¹⁹⁻²³. For example shape-dependent activity of nanoceria has been demonstrated in soot oxidation²⁹. Cubes remain more stable than rods and exhibit mostly {001} facets, where the surface mobility of Ce ions can be controlled by the chemical atmosphere^{4,30}. Cubes are more reactive for CO oxidation than the major {111} facets encountered on octahedrons^{18,31}. Hence, cubes seem to

be a good compromise between reactivity, stability and a promising morphology for further development.

As shown by earlier work, cuboidal cerium oxide nanoparticles can be obtained via microwave-assisted hydrothermal synthesis working on highly alkaline medium made of a mixture of aqueous sodium and ammonium hydroxide¹⁶. By using the ability of electron tomography to solve the third dimension of the object under study, main microstructural features of these nanocubes were evidenced: existence of a cubic shape with {002} facets, {011} (faceted) edges and {111} corners. A fitting procedure applied to the external surface of the particles allowed a precise determination of their aspect ratio, also revealing that they should be considered as parallelepipeds rather than isotropic cubes, as other groups have also shown^{4, 32}. Here we chose to combine simulations and experimental data in order to provide further insights on those cuboidal nanoparticle morphological features.

2. Experimental

2.1 CeO₂ cuboidal particles microwave heating-hydrothermal synthesis assisted

Syntheses were performed using MARS-5 and Masterwave BTR microwave digestion systems (CEM and Anton-Paar Corp. respectively). Temperature was regulated by percent increments of the microwave power (300 W, 2.45 GHz frequency) and controlled by an optical fibre.

All reagents were analytical grade and use without further purification. To obtain pure cerium oxide sample, 1.74 ml of Ce(NO₃)₃ (496 g.L⁻¹) were dissolved in 50 mL of distilled water. This solution was added drop by drop at room temperature and under vigorous agitation in the basic medium (pH=14) composed by a mixture of NaOH (*carlo erba reagenti* 35%) and NH₄OH (B.T. baker 30%) and placed in a closed Teflon container (100 mL) for microwave hydrothermal synthesis (XP-1500 plus model). The system was heated at 180°C for different reaction times

ranging from 5 to 45 min and then cooled down at room temperature. The precipitate was collected by centrifugation at 5000 rpm for 10 min, washed three times with distilled water and dried overnight at 100°C. Table 1 summarizes all the information about synthesis parameters used to obtain the desired morphologies.

Table 1. Microwave-assisted synthesis conditions (45 min / 180 °C) and corresponding microstructural characterizations of pure cuboidal CeO₂ samples

Ref. sample	%NaOH/ %NH₄OH	Median cube side length (nm)	Standard deviation (nm)
Ce1	5/95	10.4	1.4
Ce2	25/75	13.3	2
Ce3	50/50	16.5	2.5
Ce4	75/25	18.5	2.5
Ce5	95/5	23.5	3.9

2.2 Characterization and measurement

Samples for transmission electron microscopy (TEM) were prepared by suspending the powders in alcohol by ultrasonication and depositing a drop of the suspension on a copper grid covered with a carbon film. The grid was finally air-dried for 15 min. TEM, high-resolution TEM (HRTEM) experiments were performed on a JEOL 2200 FS equipped with a field emission gun operating at 200 kV with a point-to-point resolution of 0.23 nm. High-resolution micrographs and

videos were acquired with a Gatan Ultrascan CCD 2kx2k camera and digital diffractograms and calculated with the Gatan Digital Micrograph software. Moreover, in order to be representative and statistically meaningful, many images from several regions of various samples were recorded and the most characteristic results are presented here.

The different compounds were characterized by X-Ray powder diffraction (XRD) using a Philips PW 1050 diffractometer in a Bragg-Brentano geometry with Cu KR radiations of 1.54059 and 1.54441 Å (KR1 and KR2 respectively). The intensity data were collected at room temperature over a 2θ range of 8-80° with 0.02 steps and an integration time of 70 sec. Pattern profile matching was performed with the FULLPROF program³³.

2.3 Molecular Modelling

Molecular dynamics calculations use the potential model of Minervini *et al.*³⁴ and are carried out using the DL_POLY code³⁵. Model structures are made using the METADISE code³⁶.

The minimized bulk structure was cut along Miller indices to obtain the {111}, {011}, and {100} surfaces. 3D boundary conditions were used throughout, and hence, the surfaces were modelled using the slab method³⁷ in which a finite number of crystal layers is used to generate two identical surfaces via the introduction of a vacuum gap (~40 Å) perpendicular to the surface to minimize the interaction between images. The {100} and {110} slabs with a $p(4 \times 4)$ and $p(4 \times 3)$ expansion of the surface unit cell included 10 and 12 repeat units respectively, while the {111} slab with a $p(3 \times 4)$ expansion included 8 repeat units. The 3 outermost layers of each slabs are allowed to relax whereas the middle of the slab is kept fixed. All slabs were equilibrated in the temperature range of 1500 K – 3600 K at 300 K intervals for 0.5 ns with a time step of 1 fs in an NVT ensemble using the Nose - Hoover thermostat. All equilibrated configurations were then run for extra 5 ns allowing for data collection.

The generation of a model of a ceria cuboidal nanoparticle with molecular dynamics simulations has been achieved by simulating amorphisation and re-crystallization (A&R)^{1,4,38}. However this has not been trivial, as the ceria nanoparticles naturally crystallize exposing the most stable {111} surface, rendering a polyhedral shape. In order to avoid this, a crystalline seed of fluorite structure with cubic shape has been used in order to direct the crystallization. A cube of CeO₂ comprising of 20736 atoms (6912 Ce atoms, 13824 O atoms) (Fig. 1a) was melted holding fixed a cubic seed comprising of 12000 atoms (4000 Ce, 8000 O) in the centre of the nanoparticle performing constant volume MD at 8000 K for 50 ps (Fig. 1b). Crystallization was then performed applying constant volume MD simulation at 1500 K for 300 ps, allowing the atoms of the seed to move (Fig. 1c). The nanocube has then been annealed performing constant volume MD at 3750 K for 28 ns. During this time the eventual transition to a polyhedral shape has not been observed, supporting the relative stability of the cuboidal shape observed experimentally. The nanoparticle was then cooled down performing constant volume MD at 1K for 20 ps (Fig. 1d). All A&R simulations used a time step of 4 fs in an NVT ensemble using the Nose - Hoover thermostat.

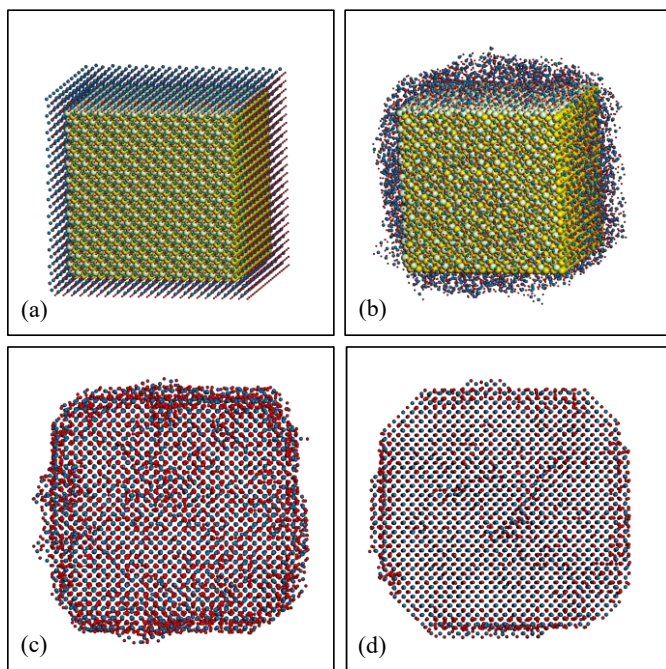


Figure 1. Amorphisation and crystallization of a ceria cubic nanoparticle; a) a pristine cube of fluorite CeO₂ structure; b) amorphisation of the ceria nanoparticle, while a cubic crystalline seed is held fixed; c) crystallization of the nanoparticle; all atoms were allowed to move; d) final structure of the cuboidal ceria nanoparticle after annealing and cooling down. A projection along the <100> direction of the crystal is shown.

3. Results and discussions

3.1 (Micro)structural characterizations

Pure ceria cuboid particles obtained by microwave-assisted hydrothermal synthesis are shown on Fig. 2. As expected they exhibit single crystalline structure (see the <001> zone axis oriented digital diffractogram on Fig. 2) and {001} lateral facets are enclosed by {011} flat edges and {111} corners. Particles account for cubes or rectangles in projection depending on the <001> zone axis they are imaged along confirming their cuboidal nature. These HRTEM images are consistent with previously reported HRTEM images for cuboidal ceria nanoparticles found in the literature^{6,29,30}.

Figure 3 shows the size distributions of ceria particles. They were obtained by counting more than a hundred particles from TEM images for each sample and the measured particle size corresponds to an average of both projected sides for each cuboid. Mean particle sizes range from 10.4 to 23.5 nm with increasing NaOH/NH₄OH bases ratio while standard deviation enlarges (Fig. 3) from 13.5% to 16.6%. One has to note the obvious effect of stirring, as the solvent becomes viscous with increasing NaOH proportion. Particles prepared via a synthesis route using a more efficient stirring (Anton-Paar Masterwave BTR system), due to differences in reactor volume and shape, show a decrease in median and average size (see orange and purple histograms on Fig. 3), compared to the same synthesis conditions, but with a less effective stirring. This indicates that a better stirring favours nucleation at the expense of growth of the particles. This feature has to be

taken in account for future microwave-assisted syntheses, when one is targeting a given particle size.

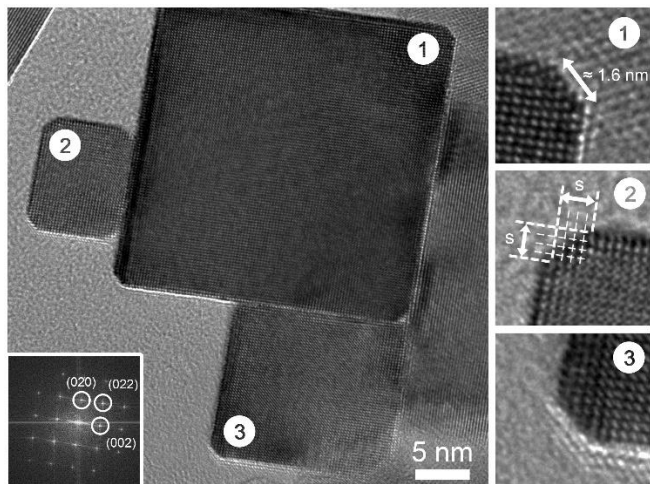


Figure 2. HRTEM micrograph of pure CeO_2 cuboidal nanoparticles (sample Ce1) and its corresponding FFT (inset). Cube edges and corners share a 1.6 nm side (diagonal of a s side square)

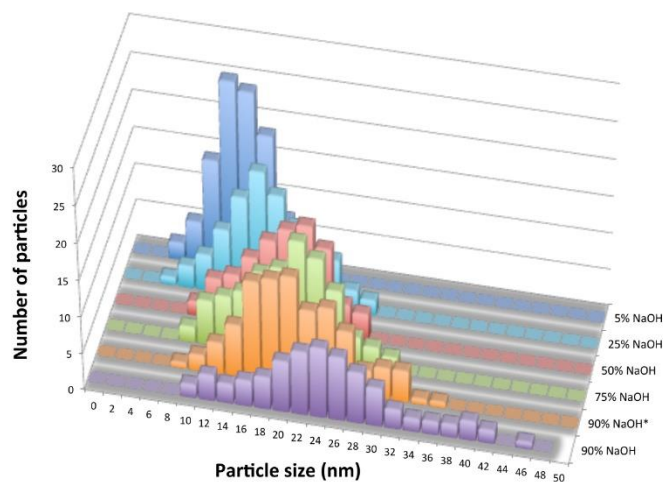


Figure 3. (Color online) Side-length distributions of pure CeO_2 cuboidal nanoparticles synthesized using $\text{NH}_4\text{OH}/\text{NaOH}$ mixture as solvent / *: particles prepared with a higher stirring efficiency

Furthermore, whatever the particle might be, projected edges and corners width remains constant and corresponds to the diagonal of a four by four square formed by $\{002\}$ planes (see the three

cuboids on Fig. 2). If we consider particles as perfect cubes with a as the cube length and c the truncation width, facets, edges and corners surfaces can be written as follows:

$$\{001\}_{area} = 6. (a - \sqrt{2}. c)^2 \quad (1)$$

$$\{011\}_{area} = 12. c. (a - \sqrt{2}. c) \quad (2)$$

$$\{111\}_{area} = 2\sqrt{3}. c^2 \quad (3)$$

Calculated contributions of those three surfaces to the overall particle area are plotted on Fig. 4. By keeping constant the size of the truncation, $\{001\}_{area}/\{011\}_{area}$ ratio can be modulated from approximately 2.1 to 9.1 for smaller and larger cuboids respectively. The low energy $\{111\}$ planes corresponding to cubes corners represent 5.1% of the cube surface for 5 nm-sized particles and can be lowered to 0.2% when the size is reaching 30 nm. It is worth noting that these values seem to adopt an asymptotic behaviour and can no longer be significantly adjusted for cuboid sizes beyond 30 nm. This suggests that a particle size of 30 nm may be a cut off for exploitation of enhanced catalytic activity. This "critical size" sees nanoparticles that are large enough to have a significant portion of the $\{100\}$ surface, but they are still small enough to have a sufficient total surface area, *i.e.* high surface to volume ratio, ideal for catalysis^{15,29,39,40}.

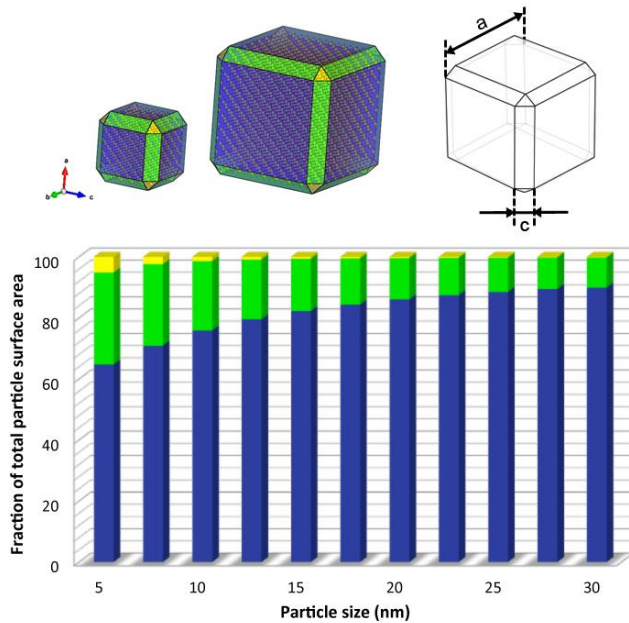


Figure 4. (Color online) Typical 3D cube models showing $\{001\}$ faces (blue), $\{011\}$ edges (green) and $\{111\}$ corners (yellow) and their calculated contribution to the total particle surface as a function of the cube side length a ($c=1.6$ nm with respect to Figure 2)

3.2 Surfaces characterization.

We show the surface structure of ceria nanocubes characterized by HRTEM (Fig. 5a). The faceting of the lateral facet of a cube (Fig. 5b) show a characteristic irregular $\{111\}/\{110\}$ sub-faceting in the $\{110\}$ mean surface plane. The faceting observed here is consistent with other studies of ceria nanoparticles in the literature, which observed faceting of both nanorods enclosed by $\{110\}$ surfaces²⁰, nanopowders²¹ and nanocubes^{15,22,30}.

In Fig. 5c the surface morphology of the simulated ceria cuboidal nanoparticle is shown. The cuboidal nanoparticle exposes mostly the $\{100\}$ surface and it is truncated at the edge and corners exposing $\{110\}$ and $\{111\}$ surfaces, respectively. However, the simulations reveal that the edges are not wholly flat, but faceted^{40,41}: the $\{110\}$ surface in this case can be described as a faceted $\{111\}/\{110\}$ (Fig. 5d). In Fig. 5e and 5f two projection along the $\langle 111 \rangle$ and $\langle 100 \rangle$ directions of

the crystal respectively are shown; corrugation (*i.e.* faceting) at the edges is visible for the projection along the $\langle 111 \rangle$ direction. The lengths of all projected corners of the model have been measured, being between 1.5 and 1.7 nm, in agreement with experiments. This minimum length of projected edges and corners stabilizes the cuboidal morphology; it is five times the inter-planar spacing of the $\{111\}$ surface (0.32 nm^2) as pointed out by both experiments and simulations. As this minimal length is a necessary requirement to stabilize the cube, it is not proportional/dependent to the size of the cube. As a consequence all corners must have at least three sides that are no smaller than 1.6 nm (Fig. 5c-f).

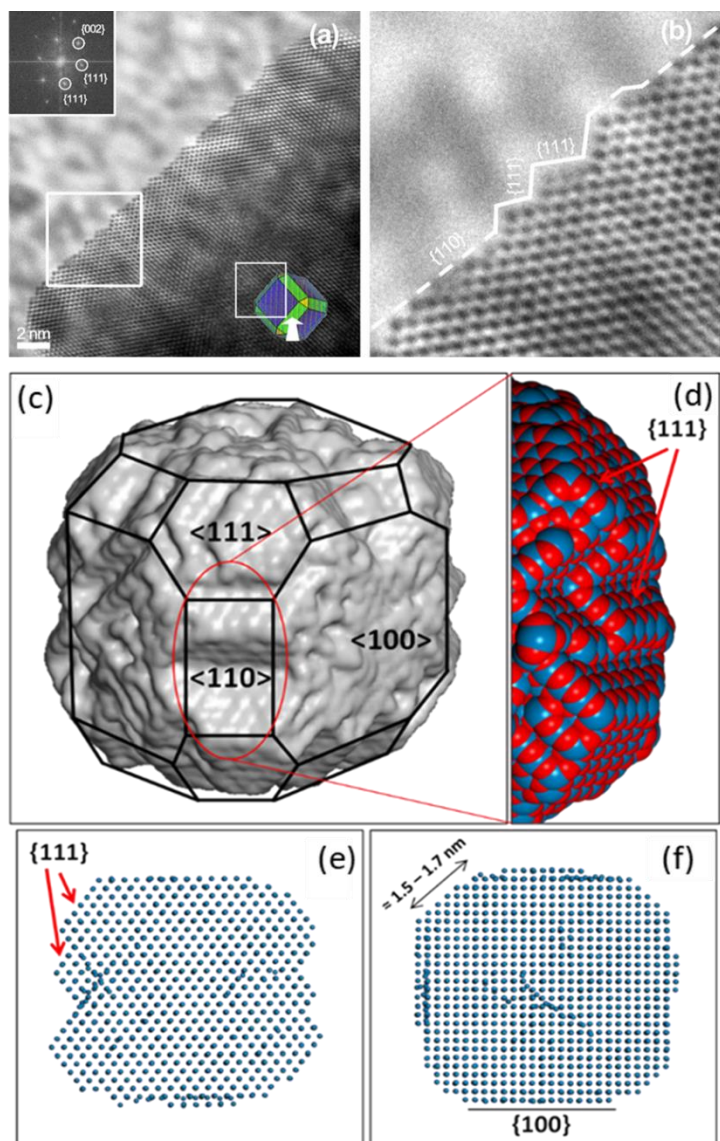


Figure 5. (a) HRTEM micrograph of a lateral facet of a cube (Ce5 sample) along a $\langle 110 \rangle$ zone axis and its corresponding digital diffractogram (inset); b) Zoomed in section of image in a) to highlight the faceting of the nanocube; c) surface rendered fully atomistic model of the ceria cuboidal nanoparticle showing the $\langle 100 \rangle$, $\langle 110 \rangle$ and $\langle 111 \rangle$ surfaces; d) enlarged segment of the edge of the cuboidal nanoparticle, showing faceted $\langle 110 \rangle$ surface; e) and f) projections along $\langle 111 \rangle$ and $\langle 100 \rangle$ directions respectively.

To confirm the existence of $\{111\}/\{110\}$ faceting on the $\{110\}$, we have performed MD calculations on the three surface, i.e. $\{100\}$, $\{110\}$ and $\{111\}$ separately. The $\{111\}$ surface shows no faceting or reconstruction at any temperature, whereas the $\{100\}$ shows a very mobile liquid-like surface layer with both the Ce and O ions being highly mobile^{1, 43}.

The $\{100\}$ surface is the most unstable of the three low Miller Index surfaces of ceria, with the order of stability being $\{111\} > \{110\} > \{100\}$ ⁴⁴. According to the Tasker notation⁴⁵, the $\{110\}$ is a type 1 surface, the $\{111\}$ is a type 2 surface and the $\{100\}$ is a type 3 surface. The type 1 $\{110\}$ surface is neutral with double O species per cation on each plane, which also correspond to the surface repeat unit. The type 2 $\{111\}$ surfaces has charged planes, although the surface repeat unit is charge neutral, thus there is no dipole moment perpendicular to the surface. Both these surfaces show relatively low surface energy, with the $\{111\}$ surface displaying the lowest as it contains 7-fold coordinated surface Ce cations, compared to the 6-fold coordinated surface Ce cations on the $\{110\}$ surface. The type 3 $\{100\}$ surface is charged and has a dipole moment in the repeat surface unit perpendicular to the surface. Type 3 surfaces are stabilized by reconstruction to quench the dipole. This reconstruction occurs in our MD simulations. The liquid-like behavior of the $\{100\}$ surface arises from the flexibility of the surface oxygen network, and so of the surface Ce ions, which can easily access many different surface oxygen arrangements due to very small energy differences between these arrangements⁴³. The $\{110\}$ and the $\{111\}$ surfaces do not display this behavior and as such they do not show a liquid-like diffusion behavior.

The origin of the faceting is a balance between the surface energy of the ceria surface which follows the $\{100\} > \{110\} > \{111\}$ and the heat of reduction of the surface which follows the $\{111\} > \{100\} > \{110\}$ ⁴⁴. As the $\{111\}$ surface is the most stable any surface that undergoes faceting will favour its appearance followed by the $\{110\}$. However it is only the $\{110\}$ surface

that undergoes faceting due to the ease of removing oxygen from its outermost layer. Visual inspections shows that oxygen species pop out the pristine flat surface and build up small ridges that then tend to crystallize into the faceted $\{111\}/\{110\}$ surface as Ce species are following the move. We noticed that faceting only occurs for the $\{110\}$ surface at temperature above 2400 K.

We can use the inter-planar spacing values for the $\{111\}$, $\{110\}$ and $\{100\}$ surfaces to define the surface unit areas of the pristine flat $\{110\}$ surface and the faceted $\{110\}/\{111\}$ surface:

$$A_{Flat\{110\}} = \left[\left(2n_{surf,Ce}^{\{110\}} - 2 \right) * |100| \right] * |110| \quad (4)$$

$$A_{Faceted\{110\}/\{111\}} = \left[\left(\sum^{\{111\}} \left(n_{surf,Ce}^{\{111\}} - 1 \right) * |111| \right) + \left(\sum^{\{110\}} A_{Flat\{110\}} \right) \right] \quad (5)$$

$n_{surf,Ce}^{\{hkl\}}$ is the number of Ce ions (must be > 1) present at the $\{hkl\}$ surface and $|hkl|$ represents the inter-planar spacing of the $\{hkl\}$ surface (*i.e.* 0.32 nm, 0.19 nm and 0.27 nm for the $\{111\}$, $\{110\}$ and $\{100\}$ surfaces respectively⁴²). For the faceted surface the total area is a summation $\sum^{\{hkl\}}$ of all the $\{hkl\}$ surface facets (*i.e.* the $\{111\}$ and $\{110\}$ surfaces that make up the faceting. Figure 6 shows schematics of different faceting all showing the relationship between inter-planar spacing and surface.

The difference between the surface unit area of the pristine flat $\{110\}$ surface and the faceted $\{110\}/\{111\}$ surface gives the excess surface unit area gained by the nanoparticle:

$$\delta A_{excess\{110\}} = A_{Faceted\{110\}} - A_{Flat\{110\}} \quad (6)$$

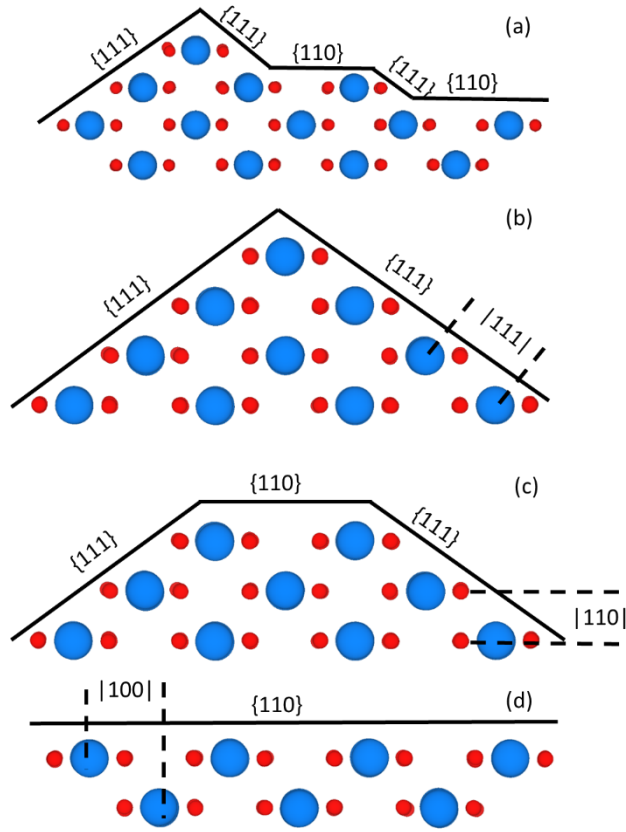


Figure 6. Schematic of different surface facets. a) $A_{Faceted \{110\}/\{111\}} = [(4 * |111|) + (4 * |100|)] * |110|$, b) $A_{Faceted \{110\}/\{111\}} = [(6 * |111|)] * |110|$ c) $A_{Faceted \{110\}/\{111\}} = [(4 * |111|) + (2 * |100|)] * |110|$, compared to d) a constant $A_{Flat \{110\}} = [6 * |100|] * |110|$.

3.3 Dynamic mobility of ions at the surface.

The mobility of ions on the surface of the ceria nanocube during the MD annealing simulation has been monitored using graphical techniques. The high temperature of annealing of 3750K was used to accelerate the dynamics to simulate what might happen over a longer timescale than ns that is typically accessible to MD simulations. In Fig. 7(a-f), snapshots of the ceria nanocube during this simulation are reported: truncated edges and corners exposing the {110} and {111} surfaces respectively are formed in the early stages of the simulation, Fig. 7b, yet their size remains

constant throughout the simulation. Cerium ions in the $\{100\}$ surface has been noted to have an increased mobility compared with the ions in the $\{110\}$ and $\{111\}$ surfaces. During the simulation dynamic exchange of ions between the surfaces occurs; in Fig. 8a section of the nanocube is shown along one of the edges and two cerium ions have been coloured differently to improve the visualization of their mobility. As it can be seen from the sequence of images, Fig. 8a – d, the cerium ion coloured in yellow move from the $\{100\}$ surface to the $\{110\}$, and at the same time the cerium ion coloured in red move from the $\{110\}$ to the $\{100\}$, keeping constant the length of the truncation at the edge. Cubes, which are a metastable morphology of ceria nanoparticles, eventually will turn to polyhedral morphologies if subjected to thermal treatments²⁹.

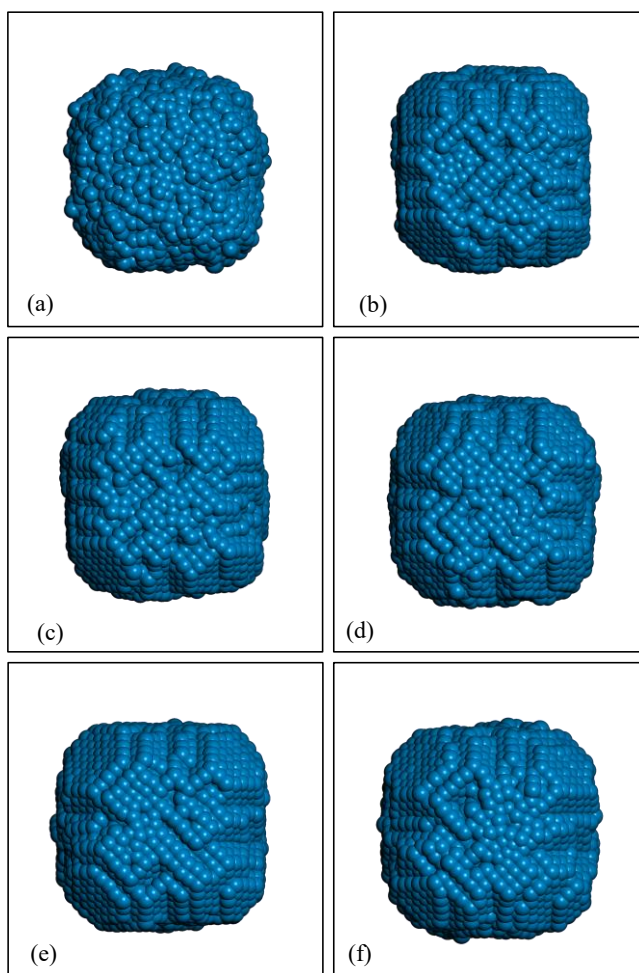


Figure 7. Annealing simulation at 3750K after a) 0 ns; b) 1.2 ns; c) 2.5 ns; d) 7.5 ns; e) 15 ns; f) 25 ns.

The diffusion of surface oxygen species affects surface structure and availability of oxygen species to catalytic activity⁴⁶. To note is the liquid-like behaviour of the {100} surface. Indeed oxygen diffuses faster on the intrinsically defective {100} surface compared to the {110} and {111} surfaces^{1,43}. At 2400 K oxygen diffusion at the {100} surface is 1 and 5 order of magnitude higher than on the {110} and {111} surfaces; these remain at 1 order of magnitude higher for the {110} and reduce to 2 orders of magnitude higher for the {111}, at 3600 K, compared to the {100}.

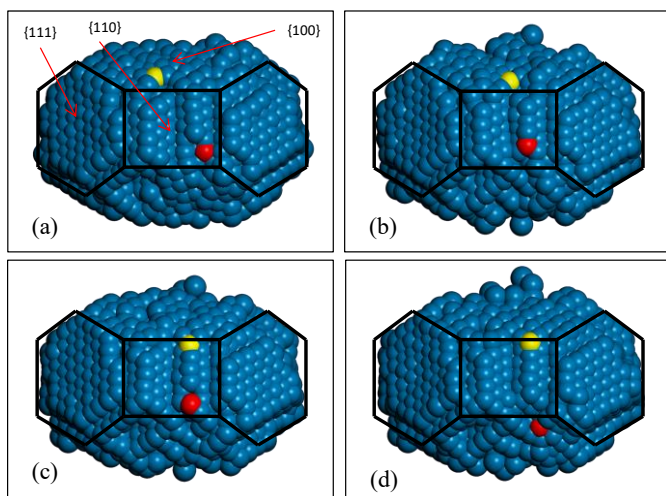


Figure 8. Section of the nanocube along one of the edges showing the dynamic mobility of cerium ions at a) 25.0 ns; b) 25.7 ns; c) 26.0 ns; d) 26.3 ns.

4. Conclusions

Nanocubes express the {100} surface with {111} corners and {110} edges. By adjusting the $\text{NH}_4\text{OH}/\text{NaOH}$ ratio during hydrothermal microwave-assisted synthesis, the distribution of {011} edges and {111} corners contributions to the total particle surface of cuboidal morphology can be modulated.

HRTEM and molecular dynamics calculations provide evidence that there is a minimum length of the {110} edges, which is 5 times (~1.6nm) the inter-planar spacing of the {111} surface, independently on particle size. Furthermore the {110} surfaces are faceted surfaces expressing {111} facets. This increases the nanoparticle surface areas proportionally to the inter-planar spacing of the {111} surface.

These findings allow for a better understanding of the surface chemistry of nanoceria, and gives ways to a rationalization of the design and engineering of active surfaces for materials design, particularly in views of face-selective catalysis⁶.

Future work should focus on testing the catalytic activity of these morphologies as well as on the effect of a chemical atmosphere on the structural changes of nanocubes synthesized via simulated amorphisation and re-crystallization and via hydrothermal microwave-assisted synthesis.

Acknowledgements

The authors would like to thank the PLACAMAT structure (University of Bordeaux-CNRS) for its electron microscopy facilities and the Anton-Paar company for its efficient scientific support. EPSRC (EP/R010366/1); Collaborative Computational Project 5 (CCP5) funded via EPSRC (EP/J010480/1); Orion Computing facility at the University of Huddersfield; ARCHER UK National Supercomputing Service (<http://www.archer.ac.uk>) via the HEC Materials Chemistry Consortium funded via EPSRC (EP/L000202, EP/R029431); THOMAS, UK Materials and Molecular Modelling Hub (MMM Hub) for computational resources (EPSRC - EP/P020194/1).

Notes and references

Corresponding authors: *

M. Molinari - M.Molinari@hud.ac.uk

J. Majimel - majimel@icmcb-bordeaux.cnrs.fr

Conflict of Interest

There are no conflicts to declare.

Author Contributions

R.L.N., F.C. and D.C.S. performed the amorphisation and re-crystallization molecular modelling calculations. R.C., B.J.P., J.M.F. and M.M. provided the surface modelling calculations. U.C., C.F-M., A.D. and J.M. provided the experimental data. All authors reviewed the manuscript.

References

1. Sayle, T. X. T. ; Molinari, M.; Das, S.; Bhatta, U.M.; Mobus, G.; Parker, S.C.; Seal S.; Sayle, D.C., Environment-mediated structure, surface redox activity and reactivity of ceria nanoparticles, *Nanoscale*, 2013, 5, 6063-6073.
2. Morgan, L. M.; Molinari, M.; Corrias, A.; Sayle, D.C., Protecting Ceria Nanocatalysts – The Role of Sacrificial Barriers, *Applied Materials & Interfaces*, 2018, 10, 32510-32515, DOI: 10.1021/acsami.8b08674.
3. Rodriguez, J.A.; Grinter, D.C.; Liu, Z.; Palomino, R.M.; Senanayaka, S.D., Ceria-based model catalysts: fundamental studies on the importance of the metal–ceria interface in

CO oxidation, the water–gas shift, CO₂ hydrogenation, and methane and alcohol reforming, *Chem. Soc. Rev.*, 2017, 46, 1824-1841.

4. Bhatta, U.M.; Reid, D.; Sakthivel, T.; Sayle, T.X.T.; Sayle, D.; Molinari, M.; Parker, S.C.; Ross, I.M.; Seal, S.; Möbus, G., Morphology and Surface Analysis of Pure and Doped Cuboidal Ceria Nanoparticles, *J. Phys. Chem. C*, 2013, 117, 24561-24569.
5. Li, Y.; Shen, W., Morphology-dependent nanocatalysts: Rod-shaped oxides, *Chem. Soc. Rev.*, 2014, 43, 1543-1574.
6. Trovarelli, A.; Llorca, J. Ceria Catalysts at Nanoscale: How Do Crystal Shapes Shape Catalysis?, *ACS Catal.*, 2017, 7, 4716-4735.
7. Lee, H., *RSC Adv.*, Utilization of shape-controlled nanoparticles as catalysts with enhanced activity and selectivity, 2014, 4, 41017.
8. Sayle, T.X.T; Cantoni, M.; Bhatta, U.M.; Parker, S.C.; Hall, S.R.; Möbus, G.; Molinari, M.; Reid, D.; Seal, S.; Sayle, D.C., Strain and Architecture-Tuned Reactivity in Ceria Nanostructures; Enhanced Catalytic Oxidation of CO to CO₂, *Chem. Mater.*, 2012, 24, 1811-1821.
9. Sayle, T. X. T. ; Inkson, B.J.; Karakoti, A.; Kumar, A.; Molinari, M.; Möbus, G.; Parker, S.C.; Seal, S.; Sayle, D.C., Mechanical properties of ceria nanorods and nanochains; the effect of dislocations, grain-boundaries and oriented attachment, *Nanoscale*, 2011, 3, 1823-1837.

10. in *Studies in Environmental Science*, ed. T. T. E. A. John Chandler, Jan Hartlén, Ole Hjelm, David S. Kosson, Steven E. Sawell, Hans A. van der Sloot, Jürgen Vehlow, Elsevier, 1997, 67, pp. 1-974.
11. Karakoti, A.; Singh, S.; Dowding, J.M.; Seal, S.; Self, W.T., Redox-active radical scavenging nanomaterials, *Chem. Soc. Rev.*, 2010, 39, 4422-4432.
12. Sreeremya, T.S.; Krishnan, A.; Remani, K.C.; Patil, K.R.; Brougham, D.F.; Ghosh, S., Shape-Selective Oriented Cerium Oxide Nanocrystals Permit Assessment of the Effect of the Exposed Facets on Catalytic Activity and Oxygen Storage Capacity, *Applied Materials & Interfaces*, 2015, 7, 8545-8555.
13. Zhang, J.; Kumagai, H.; Yamamura, K.; Ohara, S.; Takami, S.; Morikawa, A.; Shinjoh, H.; Kaneko, K.; Adschiri, T.; Suda, A., Extra-low-temperature oxygen storage capacity of CeO₂ nanocrystals with cubic facets, *Nano Lett.*, 2011, 11, 361-364.
14. Trovarelli, A., *Catalysis by Ceria and Related Materials*, Imperial College Press 2nd edn., 2013.
15. Tinoco, M.; Fernandez-Garcia, S.; Lopez-Haro, M.; Hungria, A.B.; Chen, A.; Blanco, G.; Perez-Omil, J.A.; Collins, S.E.; Okunko, H.; Calcino, J.J., Critical Influence of Nanofaceting on the Preparation and Performance of Supported Gold Catalysts, *ACS Catal.*, 2015, 5, 3504-3513.

16. Florea, I.; Feral-Martin, C.; Majimel, J.; Ihiwakrim, D.; Hirlimann, C.; Ersen, O., Three-Dimensional Tomographic Analyses of CeO₂ Nanoparticles, *Gro. Des.*, 2013, 13, 1110-1121.
17. Si, R.; Flytzani-Stephanopoulos, M., Shape and crystal-plane effects of nanoscale ceria on the activity of Au-CeO₂ catalysts for the water-gas shift reaction, *Angew. Chem. Int. Ed.*, 2008, 47, 2884.
18. Mai, H.-X. ; Sun, L.-D.; Zhang, Y.-W.; Si, R.; Feng, W.; Zhang, H.-P.; Liu, H.-C.; Yan, C.-H., Shape-Selective Synthesis and Oxygen Storage Behavior of Ceria Nanopolyhedra, Nanorods, and Nanocubes, *J. Phys. Chem. B*, 2005, 109, 24380.
19. Asahina, S.; Takami, S.; Otsuka, T.; Adschiri, T.; Terasaki, O., Exploitation of Surface-Sensitive Electrons in Scanning Electron Microscopy Reveals the Formation Mechanism of New Cubic and Truncated Octahedral CeO₂ Nanoparticles, *ChemCatChem* 2011, 3.
20. Yang, C.; Yu, X.; Heißler, S.; Nefedov, A.; Colussi, S.; Llorca, J.; Trovarelli, A.; Wang, Y.; Wöll, Surface Faceting and Reconstruction of Ceria Nanoparticles, *Angew. Chem. Int. Ed.*, 2017, 56, 375-379.
21. Crozier, P.A.;, Wang, R.; Sharma, R., In situ environmental TEM studies of dynamic changes in cerium-based oxides nanoparticles during redox processes, *Ultramicroscopy*, 2008, 108, 1432-1440.
22. Lin, Y.; Wu, Z.; Wen. J.; Poeppelmeier, K.R.; Marks, L.D., Imaging the Atomic Surface Structure of CeO₂ Nanoparticles, *Nano Lett.*, 2014, 14, 191-196.

23. Li, Y.; Shen, W., Morphology-dependent nanocatalysts: Rod-shaped oxides, Chem. Soc. Rev., Chem. Soc. Rev., 2014, 43.
24. Tauster, S. J.; Fung, S. C.; Garten, R. L., Strong metal-support interactions. Group 8 noble metals supported on titanium dioxide, J. Am. Ceram. Soc., 1978, 100, 170.
25. Majimel, J.; Lamirand-Majimel, M.; Moog, I.; Feral-Martin, C.; Tréguer-Delapierre, M., Size-Dependent Stability of Supported Gold Nanostructures onto Ceria: an HRTEM Study, J. Phys. Chem. C, 2009, 113, 9275.
26. Akita, T.; Okumura, M.; Tanaka, K.; Kohyama, M.; Haruta, M., Analytical TEM observation of Au nano-particles on cerium oxide, Catal. Today, 2006, 117, 62.
27. Akita, T.; Tanaka, K.; Kohyama, M.; Haruta, M., Analytical TEM study on structural changes of Au particles on cerium oxide using a heating holder, Catal. Today, 2007, 122, 233.
28. Liotta, L. F.; Longo, A.; Macaluso, A.; Martorana, A.; Pantaleo, G.; Venezia, A.M.; Deganello, G., Influence of the SMSI effect on the catalytic activity of a Pt (1%)/CeO₂-6ZrO₂ catalyst: SAXS, XRD, XPS and TPR investigations, Applied Catalysis B: Environmental, 2004, 48, 133.
29. Aneggi, E.; Wiater, D.; de Leitenburg, C.; Llorca, J.; Trovarelli, A.; Chape-Dependant Activity of Ceria in Soot Combustion, ACS Catal., 2014, 4, 172-181.

30. Bugnet, M.; Overbury, S.H.; Wu, Z.L.; Epicier, T. Direct Visualization and Control of Atomic Mobility at {100} Surfaces of Ceria in the Environmental Transmission Electron Microscope, *Nano Lett*, 2017, 17, 7652-7658.
31. Wu, Z.; Li, M.; Overbury, S.H., On the structure dependence of CO oxidation over CeO₂ nanocrystals with well-defined surface planes, *Journal of Catalysis*, 2012, 285, 61-75.
32. Xu, X.; Saghi, Z.; Gay, R.; Möbus, G., Reconstruction of 3D morphology of polyhedral nanoparticles, *Nanotechnology*, 2007, 18.
33. Rodriguez-Carvajal, J., Recent advances in magnetic structure determination by neutron powder diffraction, *Physica B*, 1993, 192.
34. Minervini, L.; Zacate, M.O.; Grimes, R.W., Defect cluster formation in M₂O₃-doped CeO₂, *Solid State Ionics*, 1999, 116, 339-349.
35. Smith, W.; Forester, T.R., DL_POLY_2.0: A general-purpose parallel molecular dynamics simulation package, *Journal of Molecular Graphics*, 1996, 14, 136-141.
36. Watson, G. W.; Kelsey, E.T.; deLeeuw, N.H.; Harris, D.J.; Parker, S.C., Atomistic simulation of dislocations, surfaces and interfaces in MgO, *J. Chem. Soc., Faraday Trans.*, 1996, 92, 433-438.
37. Oliver, P.M.; Parker, S.C.; Mackrodt, W.C., Computer simulation of the morphology of NiO, *Modelling and Simulation in Materials Science and Engineering*, 1993, 1, 755-760.

38. Sayle, T. X. T.; Parker, S.C.; Sayle, D.C., Shape of CeO₂ nanoparticles using simulated amorphisation and recrystallisation, *Chem. Commun.*, 2004, 21, 2438-2439, DOI: 10.1039/b408752f
39. Vile, G.; Colussi, S.; Krumeich, F.; Trovarelli, A.; Perez-Ramirez, J., Opposite Facve Sensitivity in CeO₂ in Hydrogenation and Oxidation Catalysis, *Angew. Chem. Int. Ed.*, 2014, 53, 12069-12072.
40. Bezkrvnyj, O. S.; Kraszkieicz, P.; Ptak, M.; Kepinski, L., Thermally induced reconstruction of ceria nanocubes into zigzag {111}-nanofaceted structures and its influence on catalytic activity in CO oxidation, *Catalysis Communications*, 2018, 117, 94-98.
41. Cao, Y.; Zhao, L.; Gutmann, T.; Xu, Y.; Dong, L.; Buntkowsky, G.; Gao, F.; Getting Insights into the Influence of Crystal Plane Effect of Shaped Ceria on Their Catalytic Performances, *J. Phys. Chem. C*, 2018, 122, 20402-20429.
42. Jeyaranjan, A.; Sakthivel, T.S.; Molinari, M.; Sayle D.C.; Seal, S., Morphology and Crystal Planes Effects on Supercapacitance of CeO₂ Nanostructures: Electrochemical and Molecular Dynamics Studies, *Part. Part. Syst. Char.*, 2018, 9, 1800176, DOI: 10.1002/ppsc.201800176.
43. Mullins, D.R., The surface chemistry of cerium oxide, *Surf. Sci. Rep.*, 2015, 70, 42-85.

44. Molinari, M.; Parker, S.C.; Sayle, D.C.; Islam, M.S., Water Adsorption and Its Effect on the Stability of Low Index Stoichiometric and Reduced Surfaces of Ceria, *J. Phys. Chem. C*, 2012, 116, 7073-7082.
45. Tasker, P.W., The stability of ionic crystal surfaces, *J. Phys. C: Solid State Phys.* 1979, 12, 4977-4984.
46. Lawrence, N.J.; Brewer, J.R.; Wang, L.; Wu, T-S.; Wells-Kingbury, J.; Ihrig, M.M.; Wang, G.; Soo, Y-L.; Mei, W-N.; Cheung, C.L., Defect Engineering in Cubic Cerium Oxide Nanostructures for Catalytic Oxidation, *Nano Lett.*, 2011, 11, 2666-2671

TOC Graphic

